Computer Vision and Image Understanding 152 (2016) 29–40

Contents lists available at ScienceDirect

Computer Vision and Image Understanding

journal homepage: www.elsevier.com/locate/cviu

Image segmentation using the level set and improved-variation smoothing

Kun He[a], Dan Wang[a,b,*], Xu Zhang[c]

[a] School of Computer Science, Sichuan University, No.24 in Round One Road, 610065 Chengdu, China
[b] National Key Laboratory of Fundamental Science on Synthetic Vision, Sichuan University, No.24 in Round One Road, 610065 Chengdu, China
[c] Department of Mathematics, Harbin University of Science and Technology, No.52 in Xuefu Road, 150080 Harbin, China

ARTICLE INFO

Article history:
Received 9 June 2015
Revised 7 June 2016
Accepted 29 June 2016
Available online 30 June 2016

PACS:
75.40.-s
71.20.LP

Keywords:
Image segmentation
The level set
Improved total variation
Image smoothing
Confidence level
Real image

ABSTRACT

Traditional active contour models perform poorly on real images with inhomogeneous sub-regions. In order to overcome this limitation, this paper has proposed a novel segmentation algorithm. Firstly, analyzing the smoothing conditions for image segmentation, we construct a smoothing function with improved total variation. This function can smooth the inhomogeneous sub-regions, preserve the strong edges and enhance the weak edges. Then, the level set is employed to segment the smoothing component using the smoothing function. Lastly, according to the confidence level of segmentation sub-regions, we add a convergence condition to the smoothing to prevent the segmentation curve from vanishing. Experimental results indicate that this model is insensitive to noise and can deal with inhomogeneous intensity.

1. Introduction

Region-of-interest plays an important role in various applications including medical applications (Yeo et al., 2013) and video encoding (Cha and Kim, 2005). Further, it is a critical intermediate step in machine vision. For example, to recognize a particular person in a crowd, the face sub-region need to be extracted (Wang et al., 2014). Image segmentation has the ability to extract the region-of-interest. Although this technology has been widely studied for specific applications in recent decades, it is still a challenging task for researchers and developers to develop a universal technique (Shen et al., 2014).

The classical segmentation algorithms assume that the sub-region has common characteristics (Vese and Osher, 2004), i.e. color, intensity, specific features and so on. The same specific description cannot be given for the characteristics of different objects. Further, it is easily affected by noise and sub-region texture. The noise causes pseudo-edges and weakens the differences among sub-regions, and the sub-region texture may form a weak edge or inhomogeneous sub-region. Above all, inhomogeneous sub-regions and noise are the two main factors for segmentation on real images.

The segmentation models based on active contour are popular algorithms for dividing an image into foreground (region-of-interest) and background, they basically make use of a deformable curve which conforms to various shapes of objects (Khan, 2014). From the curve representation cue, the models can be broadly classified as either parametric active contour (i.e. the snake model (Kass et al., 1988)) or geometric active contour (i.e. the level set (Chan and Vese, 2001b)). In the Snake model, the curve is parameterized by arc length in a Lagrangian framework. It is difficult for this framework to handle topological structure deformation of contour, such as the curves merging and splitting. The geometric active contour models give a solution (Tsai et al., 2001), in which the contour is represented implicitly as the zero level set of a function in an Eulerian framework (Chan and Vese, 2001a). According to the energy function of their curve evolution, the models can be broadly classified as either edge-based or region-based models (Xiao et al., 2014).The edge-based models, which use local information, are very sensitive to noise. The region-based models, which utilize the global information, can segment images with noise.

In general, the classical segmentation models can extract cartoon objects (Andersson et al., 2013). However, they can not deal with the inhomogeneous sub-regions and weak edges of real

* Corresponding author.
E-mail address: 535459443@qq.com (D. Wang).

http://dx.doi.org/10.1016/j.cviu.2016.06.006
1077-3142/

images. To smooth inhomogeneous sub-regions, a Gaussian filter (Li et al., 2005) is employed. A Gaussian filter with large standard variance may seriously blur boundaries and lead to the over-convergence of a curve. Conversely, when the Gaussian filter has a small standard variance, the curve will be premature. It is difficult to adaptively choose the standard variance of Gaussian function. The improved level set method improves the accuracy of specific object location (Yang et al., 2014) by incorporating object shape into the initial curve. The segmentation model, which combines shape and enhancing gradient features, can split images with noise and weak edges (Yeo et al., 2014).

By minimizing the Mumford-Shah smooth function (Mumford and Shah, 1989), images are decomposed into different sub-regions. However, this function is difficult to minimize due to non-convexity in general. To decrease computation costs, the CV model (Chan and Vese, 2001b) can successfully split images with homogenous sub-regions using the mean of the sub-regions. However, for real images, there is a significant difference between the segmentation curve and the ground truth. To segment inhomogeneous images, the piecewise smooth (PS) models (Vese and Chan, 2002, Tsai and Yezzi, 2001) are proposed. However, their application is limited due to their expensive computational cost. The local image fitting (LIF) model (Li and Kao, 2007) has low computational complexity. The local binary function (LBF) (Li and Kao, 2008) is proposed to segment images' inhomogeneous regions. By normalizing local image fitting energy (NLIFE) (Peng and Liu, 2012), Peng and Liu (2014) proposed a local region-based active contour model.

In order to improve the traditional segmentation models performance for real images, this paper has proposed a novel segmentation model. In this model, we analyze the smoothing conditions for segmentation, and construct a smoothing function with improved total variation inspired by the Mumford-Shah and total variation functions. This function can smooth inhomogeneous sub-regions, maintain strong edges and enhance weak edges. Then, the level set has been employed to split the smoothing component. Lastly, a convergence condition for image smoothing is built according to the confidence level of different smoothing component sub-regions, in order to avoid vanishing of the level set curve. Compared with the Chunming Li model (Li et al., 2005), the Chan and Vese model (Chan and Vese, 2001b) and the Janakiraman IMST model (Janakiraman and Chandra Mouli, 2008), experimental results show that this model is insensitive to noise, and can handle inhomogeneous intensity at the same time.

The outline of the paper is as follows. In the next section, we analyze the smoothing conditions for segmentation and construct the smoothing function using the improved total variation. Next, in Section 3, combining the improved total variation with the level set, a new image segmentation model has been proposed. The proposed model is implemented in Section 4, and a convergence condition for image smoothing is built to avoid segmentation curve vanishing. The experimental results are given in Section 5. Finally, the conclusion is given in Section 6.

2. The improved total-variation smoothing

The CV model is the curve evolution implementation of the Mumford–Shah model. The Mumford-Shah function (Mumford and Shah, 1989) is:

$$E(\boldsymbol{u}, C) = \frac{\tau}{2}\int_{\Omega} |\boldsymbol{u}_0 - \boldsymbol{u}|^2 dxdy + \int_{\Omega/C} |\nabla \boldsymbol{u}|^2 dxdy + \nu|C|) \tag{1}$$

Where u_0: $\Omega \to R$ is a given image, u is a piecewise smooth component of an image u_0, there are analogical features within a sub-region and significant differences among sub-regions. Inspired by this image representation, we give the smooth representation which satisfies the following equation:

$$E(\boldsymbol{u}) = \frac{\tau}{2}\int_{\Omega} (\boldsymbol{u} - \boldsymbol{u}_0)^2 dxdy + \int_{\Omega} \psi(|\nabla \boldsymbol{u}|) dxdy \tag{2}$$

Let us suppose that $E(\boldsymbol{u})$ in Eq. (2) has a minimum resolution $\boldsymbol{u}$, then it satisfies the Euler-Lagrange equation

$$\tau(\boldsymbol{u} - \boldsymbol{u}_0) - \nabla \cdot \psi(|\nabla \boldsymbol{u}|) = 0 \tag{3}$$

To analyze the diffusion performance of the function $\psi(|\nabla \boldsymbol{u}|)$, we are going to show that it can be decomposed using the local image structures, that is, the tangent and normal directions to the isophote lines. The diffusion performances along the tangent and normal directions are respectively denoted by ρ_T and ρ_N:

$$\rho_T = \frac{\psi'(|\nabla \boldsymbol{u}|)}{|\nabla \boldsymbol{u}|}, \quad \rho_N = \psi''(|\nabla \boldsymbol{u}|) \tag{4}$$

In order to smooth non-uniformity regions and preserve boundaries, the function $\psi(|\nabla \boldsymbol{u}|)$ may satisfy the following two conditions:

(1) At locations where the gradients are low, we would like to encourage the same smoothing speeds in both tangential and normal directions. Assuming that the function $\psi(|\nabla \boldsymbol{u}|)$ is regular, this condition may be achieved by implementing the following:

$$\lim_{|\nabla \boldsymbol{u}|\to 0} \frac{\psi'(|\nabla \boldsymbol{u}|)}{|\nabla \boldsymbol{u}|} = \lim_{|\nabla \boldsymbol{u}|\to 0} \psi''(|\nabla \boldsymbol{u}|) = \alpha > 0 \tag{5}$$

(2) In a neighborhood of an edge (strong gradients), if we want to preserve this edge, it is better to diffuse along this edge and not across it. If we want to enhance this edge, it is better to reverse diffusion along the normal direction. To do this, it is sufficient to annihilate or negative for ρ_N:

$$\lim_{|\nabla \boldsymbol{u}|\to \infty} \frac{\psi'(|\nabla \boldsymbol{u}|)}{|\nabla \boldsymbol{u}|} = \beta > 0, \quad \lim_{|\nabla \boldsymbol{u}|\to \infty} \psi''(|\nabla \boldsymbol{u}|) = \gamma \le 0 \tag{6}$$

The function $\psi(|\nabla u|) = |\nabla u|^2$ blurs image edges and satisfies the first condition, that is, the diffusion performances along the tangent and normal directions are one. To preserve edges, Rudin, Osher and Fatemi proposed total variation (Chan et al., 2001). It does not obey the first condition, that is $\rho_N \equiv 0$. According to the above, the two conditions are incompatible. By analyzing the total variation, we construct a new function.

$$\psi(|\nabla \boldsymbol{u}|) = \frac{|\nabla \boldsymbol{u}|}{\sigma^2} \exp\left(-\frac{|\nabla \boldsymbol{u}|^2}{2\sigma^2}\right) \tag{7}$$

The diffusion performances of this function are following:

$$\begin{aligned} \rho_T &= \left(\frac{1}{|\nabla \boldsymbol{u}|\sigma^2} - \frac{|\nabla \boldsymbol{u}|}{\sigma^4}\right) \exp\left(-\frac{|\nabla \boldsymbol{u}|^2}{2\sigma^2}\right), \\ \rho_N &= \left(\frac{|\nabla \boldsymbol{u}|^3}{\sigma^6} - \frac{3|\nabla \boldsymbol{u}|}{\sigma^4}\right) \exp\left(-\frac{|\nabla \boldsymbol{u}|^2}{2\sigma^2}\right) \end{aligned} \tag{8}$$

Where the variation of the intensity is weak, $\rho_T > 0$ and $\rho_N < 0$. In the neighborhood of edges ($|\nabla u| \to \infty$), both converge to zero (seen Fig 1).

The smoothing model of the improved total variation is as follows:

$$E^{(ITV)}(\boldsymbol{u}) = \frac{\tau}{2}\int_{\Omega} (\boldsymbol{u} - \boldsymbol{u}_0)^2 dxdy + \int_{\Omega} \frac{|\nabla \boldsymbol{u}|}{\sigma^2} \exp\left(-\frac{|\nabla \boldsymbol{u}|^2}{2\sigma^2}\right) dxdy \tag{9}$$

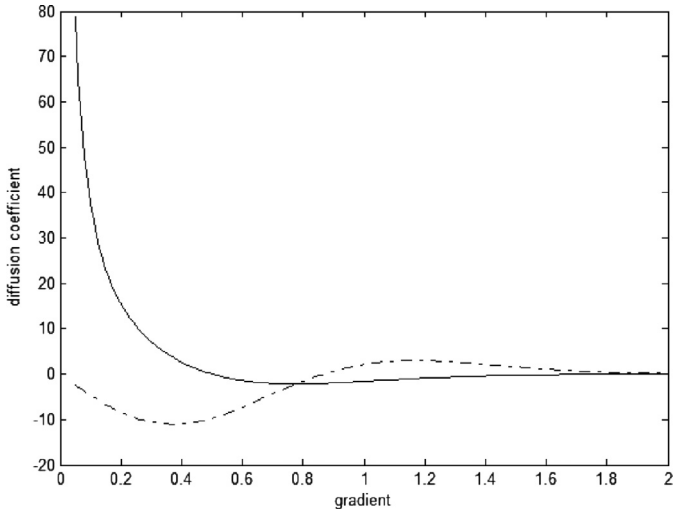

Fig. 1. The diffusion performance of the function ($\sigma = 0.5$). The solid and dash dot curve denote the diffusion in the tangent and normal direction respectively.

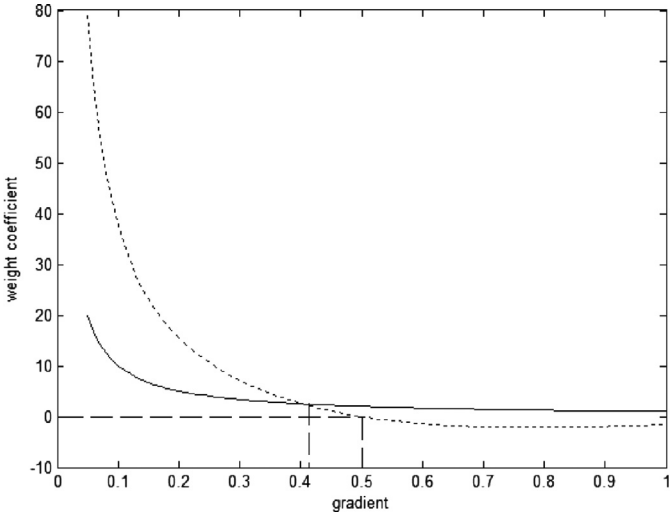

Fig. 2. The curve of weight coefficient. The solid curve denotes weight of the total variation, the dot curve represents the weight of the improved total variation with $\sigma = 0.5$.

3. Image segmentation model

The level set has been employed to segment images. It's basic idea is that contours are represented as the level set of an implicit function $\phi(x, y)$, that is $C = \{(x, y)|\phi(x, y) = 0\}$. The inside region $\{(x, y)|\phi(x, y) < 0\}$ and outside region $\{(x, y)|\phi(x, y) > 0\}$ correspond to the foreground and background. To simplify, the outside- and inside-region of the curve are approximated by the Heaviside function $H(\phi)$. The curve is represented as the one-dimensional Dirac measure $\delta(\phi)$, it is the derivative of $H(\phi)$. $H(\phi)$ and $\delta(\phi)$ are defined respectively as:

$$H(\phi) = \begin{cases} 1 & \phi \geq 0 \\ 0 & \phi < 0 \end{cases}, \quad \delta(\phi) = \frac{dH(\phi)}{d\phi} \tag{10}$$

The segmentation model using level set is minimized in the following energy function (Li et al., 2005):

$$E^{li}(\phi) = \lambda \int_\Omega g\delta(\phi)|\nabla\phi|dxdy + \nu \int_\Omega gH(-\phi)dxdy + \frac{\mu}{2}\int_\Omega (|\nabla\phi| - 1)^2 dxdy \tag{11}$$

Incorporating the improved total-variation smoothing model, the energy function of segmentation is proposed :

$$\begin{aligned} E(\phi, \boldsymbol{u}) &= E^{li}(\phi) + E^{ITV}(\boldsymbol{u}) \\ &= \lambda \int_\Omega g\delta(\phi)|\nabla\phi|dxdy + \nu \int_\Omega gH(-\phi)dxdy \\ &\quad + \frac{\mu}{2}\int_\Omega (|\nabla\phi| - 1)^2 dxdy \\ &\quad + \frac{\tau}{2}\int_\Omega (\boldsymbol{u} - \boldsymbol{u}_0)^2 dxdy + \int_\Omega \frac{|\nabla \boldsymbol{u}|}{\sigma^2} \exp\left(-\frac{|\nabla \boldsymbol{u}|^2}{2\sigma^2}\right) dxdy \end{aligned} \tag{12}$$

Where g is the edge indicator function of smoothing component $\boldsymbol{u}$, it is defined:

$$g(\boldsymbol{u}) = (1 + |\nabla \boldsymbol{u}|)^{-1} \tag{13}$$

By calculating variations, the Gateaux derivative (Evans, 1998) of the function $E(\phi, u)$ in (12) can be written as

$$\frac{\partial E(\phi, \boldsymbol{u})}{\partial \phi} = -\mu\left[\Delta\phi - \nabla \bullet \left(\frac{\nabla\phi}{|\nabla\phi|}\right)\right] - \lambda\delta(\phi)\nabla \bullet \left(g\frac{\nabla\phi}{|\nabla\phi|}\right) - \nu g\delta(\phi) \tag{14}$$

Where Δ is the Laplacican operator. By introducing an artificial temporal variable t, we use the steepest descent process to get minimization of the function $E(\phi, \boldsymbol{u})$, whose gradient flow is:

$$\frac{\partial \phi}{\partial t} = -\frac{\partial E(\boldsymbol{u}, \phi)}{\partial \phi} = \mu\left[\Delta\phi - \nabla \bullet \left(\frac{\nabla\phi}{|\nabla\phi|}\right)\right] + \lambda\delta(\phi)\nabla \bullet \left(g\frac{\nabla\phi}{|\nabla\phi|}\right) + \nu g\delta(\phi) \tag{15}$$

The smooth component $\boldsymbol{u}$ is a result of the proposed smoothing method. By applying Euler-Lagrange equation, we can obtain the diffusion equation for smoothing

$$\frac{\partial E(\phi, \boldsymbol{u})}{\partial \boldsymbol{u}} = \tau(\boldsymbol{u} - \boldsymbol{u}_0) - \nabla \cdot \left[\frac{\nabla \boldsymbol{u}}{|\nabla \boldsymbol{u}|}\left(\frac{\sigma^2 - |\nabla \boldsymbol{u}|^2}{\sigma^4}\right)\exp\left(-\frac{|\nabla \boldsymbol{u}|^2}{2\sigma^2}\right)\right] \tag{16}$$

4. Implementation

4.1. The digitization of the improved total variation smoothing

During the image smoothing, the component $\boldsymbol{u}$ in (16) contains the constant intensity sub-region in which the gradient is zero, i.e. $|\nabla \boldsymbol{u}| = 0$. To avoid this problem, we introduce a small enough positive number a ($a = 0.001$), $|\nabla \boldsymbol{u}|$ in (16) is defined as:

$$|\nabla \boldsymbol{u}|_a = \sqrt{a^2 + |\nabla \boldsymbol{u}|^2} \tag{17}$$

To compute the smoothing component, we use a semi-implicit finite difference scheme. Give the center pixel α and four neighbors region Λ, the approximation of (16) can be simply written as:

$$\boldsymbol{u}(\alpha) = \frac{1}{\tau + \sum_{p\in\Lambda}\omega(p)}\left[\tau \boldsymbol{u}_0(\alpha) + \sum_{p\in\Lambda}\omega(p)\boldsymbol{u}(p)\right] \tag{18}$$

Where

$$\omega(p) = \frac{\sigma^2 - |\nabla \boldsymbol{u}(p)|_a^2}{\sigma^4 |\nabla \boldsymbol{u}(p)|_a} \exp\left(-\frac{|\nabla \boldsymbol{u}(p)|_a^2}{2\sigma^2}\right)$$

In (18), the smoothing component contains the information of an image. If pixels p and α are located in a sub-region where the

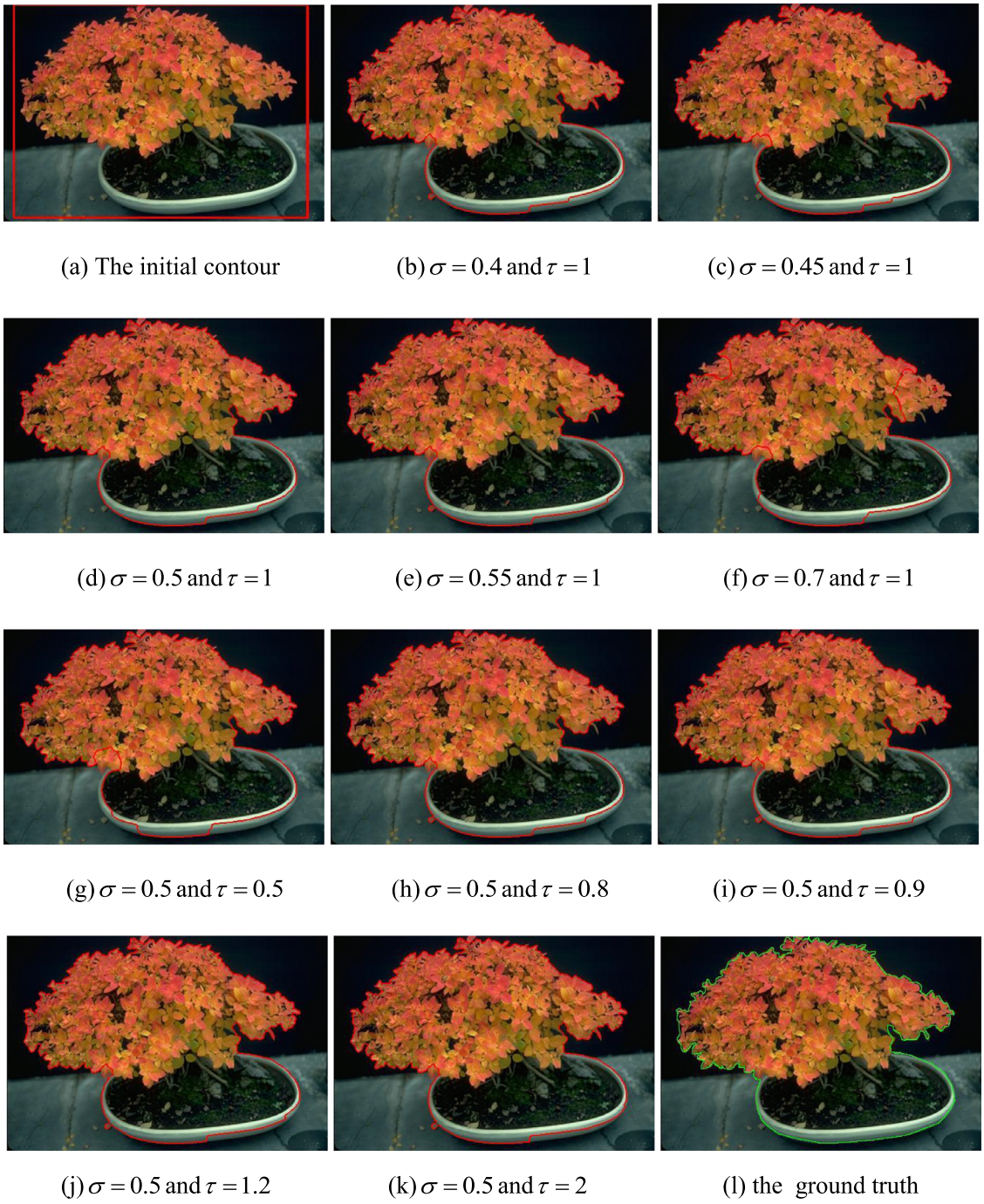

Fig. 3. Result of segmentation with different parameters.

gradients are low, the coefficient $\omega(p)$ is large, and the pixel α is the weight-sum of the neighboring pixels. If pixels p and α are located in different sub-regions, that is, $|\nabla u(p)| \to \infty$, $\omega(p)$ is negative and the edges are enhanced.

Compared with the weight of the total variation, that is $\omega^{TV}(p) = |\nabla u(p)|^{-1}$, this weight coefficient $\omega(p)$ is larger where the gradients are low. This sub-region is seriously smoothed. In the neighborhood of an edge, $\omega(p) < 0 < \omega^{TV}(p)$, this method can enhance edges where gradients are equal or greater than σ. The curves of weight coefficient on the neighbor pixel are shown in Fig 2.

4.2. Numerical scheme for the level Set

During the contour evolving, the Dirac function $\delta(\phi)$ in (14) is slightly smoothed, and $\delta_b(\phi)$ defined by:

$$\delta_b(\phi) = \begin{cases} 0 & |\phi| > b \\ \frac{1}{2b}\left[1 + \cos\left(\frac{\pi\phi}{b}\right)\right] & |\phi| \le b \end{cases} \tag{19}$$

In this paper, we use the regularized Dirac $\delta_b(\phi)$ ($b = 1.5$). The temporal partial derivative $\partial\phi/\partial t$ is approximated by the forward difference, and the spatial partial derivative $\nabla\phi = (\partial\phi/\partial x, \partial\phi/\partial y)$ is approximated by the central difference. As the above difference

(a) The initial contour (b) 10 smoothing iterations (c) 18 smoothing iterations

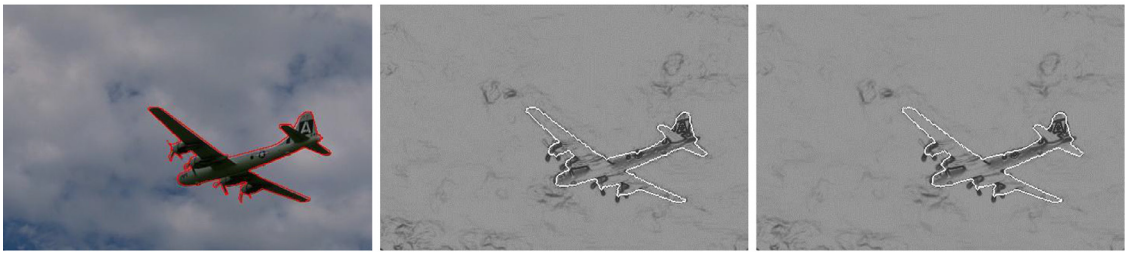

(d) The ground truth (e) Edge indicator function10^{th} (f) Edge indicator function18^{th}

Fig. 4. Result for a plane and cloud image with slightly inhomogeneous sub-regions.

(a) The initial contour (b) 30 smoothing iterations (c) 60 smoothing iterations

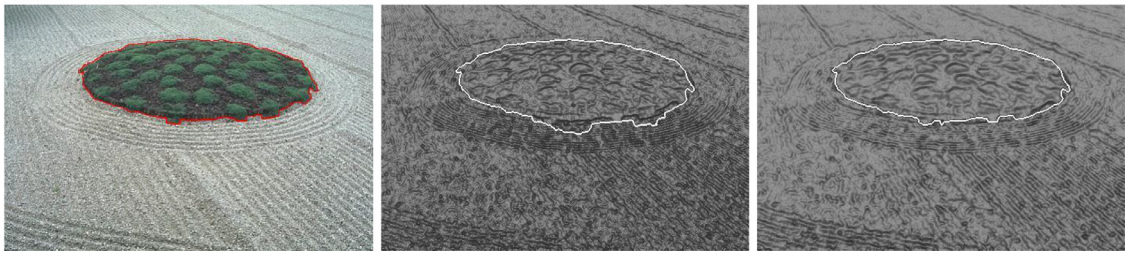

(d) The ground truth (e) Edge indicator function30^{th} (f) Edge indicator function60^{th}

Fig. 5. Result for a grass and sand image with severely inhomogeneous sub-regions.

schemes, the approximation of (14) can be simply written as:

$$\frac{\phi^{k+1}-\phi^{k}}{\Delta t}=\mu\left[\Delta\phi^{k}-\nabla\bullet\left(\frac{\nabla\phi^{k}}{|\nabla\phi^{k}|}\right)\right]+\lambda\delta_{b}(\phi^{k})\nabla\bullet\left(g(\boldsymbol{u})\frac{\nabla\phi^{k}}{|\nabla\phi^{k}|}\right)+\nu g(\boldsymbol{u})\delta_{b}(\phi^{k}) \quad (20)$$

Where, Δt is the time step.

Unfortunately, since $\lim_{|\nabla u|\to\infty}\frac{|\nabla u|}{\sigma^{2}}\exp(-\frac{|\nabla u|^{2}}{2\sigma^{2}})=0$ in (12), the smoothing component converges to the mean of the initial image, which leads to the level set curve vanishing. To avoid this phenomenon, we give the confidence level of segmentation sub-regions, it is defined as following:

$$\Pr=\frac{card(A^{N}(\phi\le 0)\cap A^{N-1}(\phi\le 0))}{\max\{card(A^{N}(\phi\le 0)),card(A^{N-1}(\phi\le 0))\}} \quad (21)$$

Here the set $A^{N}(\phi\le 0)$ represents inside region $\{(x,y)|\phi(x,y)<0\}$ and the zero level set curve $\{(x,y)|\phi(x,y)=0\}$ for the

component u^N, the set $A^{N-1}(\phi \le 0)$ of u^{N-1}. u^N and u^{N-1} are the component of the N and $N-1$ times iteration smoothing, respectively.

According to the confidence level of the segmentation sub-regions, we build the condition of convergence on the image smoothing, which is defined as:

$$\Pr \ge T \tag{22}$$

The proposed segmentation is described as follows:

program ImageSegmentation (Output)
{Initial: $\tau, \sigma, \lambda, \mu, \nu, \Delta t, T, \varphi^0(x,y)$ and $u^0 = u_0$}
N is the number of image smoothing
Begin
  N:= 0;
  Repeat
    Computing the weight coefficient $\omega(p)$ of smoothing component u^N uses:
      $\omega^N(p) = \frac{\sigma^2 - |\nabla \boldsymbol{u}^{N-1}(p)|_a^2}{\sigma^4 |\nabla \boldsymbol{u}^{N-1}(p)|_a} \exp(-\frac{|\nabla \boldsymbol{u}^{N-1}(p)|_a^2}{2\sigma^2})$; *//formula (18)*
    Computing image smoothing component u^N uses:
      $\boldsymbol{u}^N(\alpha) = \frac{1}{\tau + \sum_{p \in \Lambda} \omega(p)} [\tau \boldsymbol{u}_0(\alpha) + \sum_{p \in \Lambda} \omega(p) \boldsymbol{u}^{N-1}(p)]$; *//formula (17)*
    Computing the edge indicator function of smoothing component u^N uses:
      $g(\boldsymbol{u}^N) = \frac{1}{1 + |\nabla \boldsymbol{u}^N|}$; *//formula (13)*
    segmentation based on the level set for smoothing component u^N uses:
      //formula (20)
      $\frac{\phi^{k+1} - \phi^k}{\Delta t} = \mu[\Delta \phi^k - \nabla \bullet (\frac{\nabla \phi^k}{|\nabla \phi^k|})] + \lambda \delta_b(\phi^k) \nabla \bullet (g(\boldsymbol{u}^N) \frac{\nabla \phi^k}{|\nabla \phi^k|}) + \nu g(\boldsymbol{u}^N) \delta_b(\phi^k)$;
    Until
      The convergence condition:
        $\Pr \ge T$; *//formula (22)*
    Output: the result of segmentation.
End

5. Experimental results

The experiments are conducted using VC 6.0 on the PC with Intel-Core CPU 3.40 GHz and 4GB of RAM without any particular code optimization. The images shown in this paper are selected from the Berkeley segmentation database and the Internet. During the implementation of the proposed model, we used the parameters $\lambda = 5.0$, $\mu = 0.04$, $\nu = 3.0$, $\Delta t = 5.0$ and $T = 0.95$ for all experiments.

The image is smoothed using the improved total variation in the proposed model, and smoothing performance depends on parameters σ and τ in (16). To analyze the relationship between parameters and segmentation performance, a 480 × 320-pixel potted-tree image with inhomogeneous sub-regions (i.e. Crown region of the tree) is smoothed with different parameters, and the results of segmentation are shown as Fig. 3. When σ is small and τ is given, the regions with low gradient can be protected, leading to evolving curve under-convergence. Otherwise, the edges are smoothed and the curve has over-convergence. When τ is small and σ is given, the partial sub-regions of the object are regarded as the background region, i.e. pot region. When τ is large, the partial background is regarded as the object. The F-measure of segmentation with different parameters is listed in Table 1.

In this model, the smooth components converge to the mean of the image without constrained conditions, which can lead to disappearance of the level set curve. To validate how the smoothing number affects the segmentation performance, a 480 × 320-pixel plane and cloud image of the Berkeley segmentation database has been chosen. In this image, some sub-regions are slightly inhomogeneous. The segmentation results and corresponding edge indicator functions are shown in Fig. 4. The F-measure, precision and recall are 0.913, 0.989, and 0.847 with 18 times, respectively.

A 480 × 320-pixel grass and sand image with severely inhomogeneous sub-regions is segmented, shown as Fig. 5. F-measure, precision and recall with 60 times are 0.971, 0.984, and 0.958, respectively. Observation of different iterations of the edge indicator function shows, the smoothing method using improved total variation can preserve the edge and smooth the region with inhomogeneous intensity. With the increasing number of iterations, the difference of the edge indicator function around the boundaries is obvious.

The weak edges are a key factor affecting the segmentation performance. To test if this algorithm could handle weak edges, the result of segmentation on a 480 × 320-pixel image is shown as Fig. 6. From Fig. 6e and f, the edge indicator function becomes smaller at weak edges. It means that this method can enhance weak edges. The F-measure, precision and recall are 0.949, 0.945, and 0.952, respectively.

(a) The initial contour (b) 20 smoothing iterations (c) 35 smoothing iterations

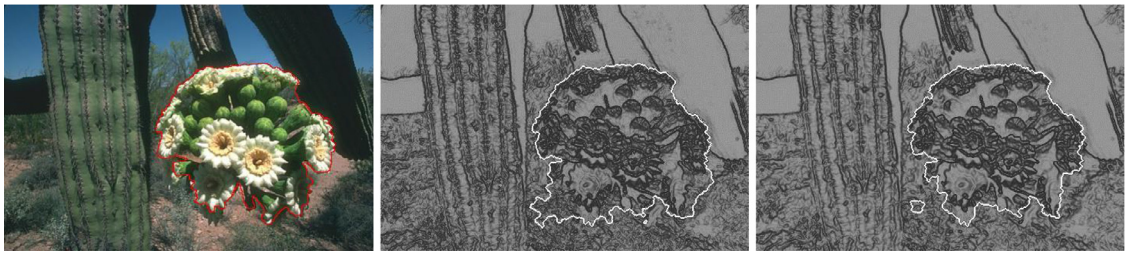

(d) The ground truth (e) Edge indicator function20th (f) Edge indicator function35th

Fig. 6. Result for a real image with weak edge.

Table 1
F-measure of image segmentation with different parameters.

τ	σ								
	0.2	0.3	0.4	0.45	0.5	0.55	0.6	0.7	1.0
0.5	0.712	0.754	0.811	0.845	0.861	0.856	0.852	0.841	0.838
0.6	0.734	0.812	0.832	0.883	0.907	0.87	0.861	0.859	0.845
0.8	0.798	0.838	0.856	0.902	0.928	0.902	0.887	0.879	0.878
0.9	0.835	0.846	0.873	0.914	0.944	0.936	0.921	0.92	0.915
1.0	0.849	0.863	0.892	0.923	0.954	0.951	0.948	0.940	0.938
1.2	0.845	0.86	0.881	0.921	0.945	0.940	0.940	0.937	0.938
1.5	0.841	0.857	0.876	0.916	0.938	0.932	0.932	0.93	0.927
2	0.839	0.855	0.87	0.912	0.937	0.930	0.928	0.926	0.922
4	0.832	0.851	0.867	0.907	0.937	0.926	0.92	0.918	0.918

a) initial curves b) the ground truth c) the proposed method

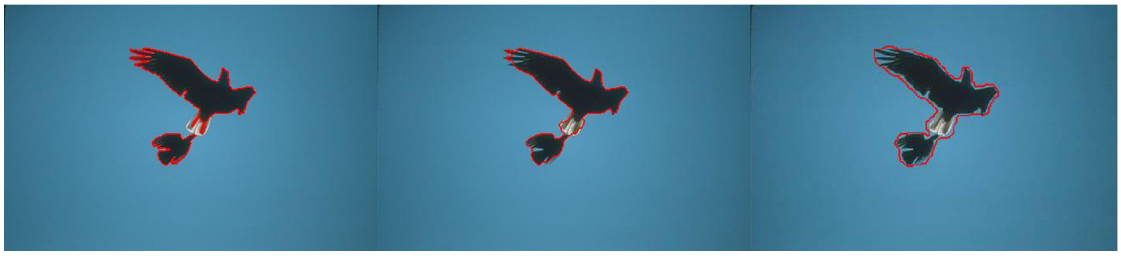

d) CV e) Li f) IMST

Fig. 7. Comparison of the segmentation method on the image 'the eagles'.

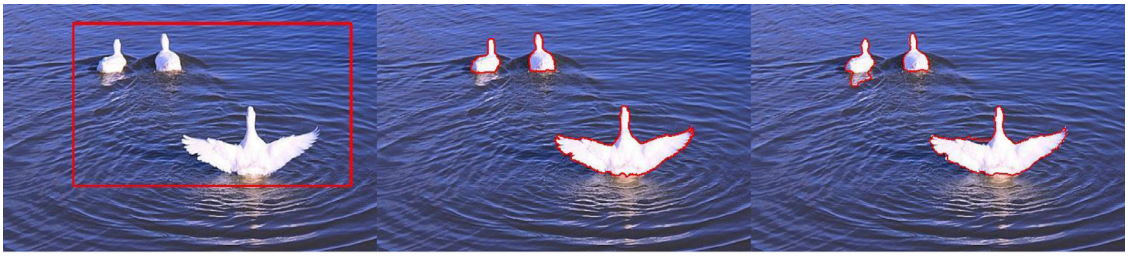

a) initial curves b) the ground truth c) the proposed method

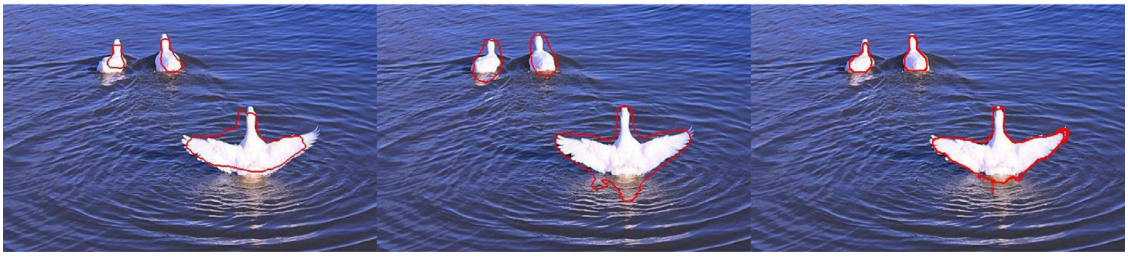

d) CV e) Li f) IMST

Fig. 8. Comparison of the segmentation method on the image 'the swans'.

Table 2
CPU time and score of segmentation comparison of Figs. 7–11.

Method	*Image and it's size*				
	Fig .7	*Fig .8*	*Fig .9*	*Fig .10*	*Fig .11*
	480×320	508×321	320×221	600×392	480×320
The proposed method precision	0.996	0.951	0.960	0.994	0.928
recall	0.871	0.877	0.930	0.951	0.856
F-measure	0.930	0.913	0.945	0.972	0.891
CPU time (s)	9.672	30.84	7.529	39.396	41.345
Li precision	0.991	0.880	0.930	0.927	0.413
recall	0.884	0.707	0.873	0.857	0.768
F-measure	0.934	0.784	0.900	0.890	0.537
CPU time (s)	8.579	24.226	6.288	28.975	24.461
CV precision	0.891	0.717	0.927	0.889	0.223
recall	0.932	0.963	0.871	0.922	0.859
F-measure	0.911	0.822	0.898	0.905	0.354
CPU time(s)	6.365	19.822	4.989	17.552	14.258
IMST precision	0.965	0.905	0.933	0.952	0.642
recall	0.854	0.864	0.896	0.932	0.866
F-measure	0.927	0.819	0.912	0.941	0.658
CPU time(s)	4.188	12.919	4.175	12.152	11.588

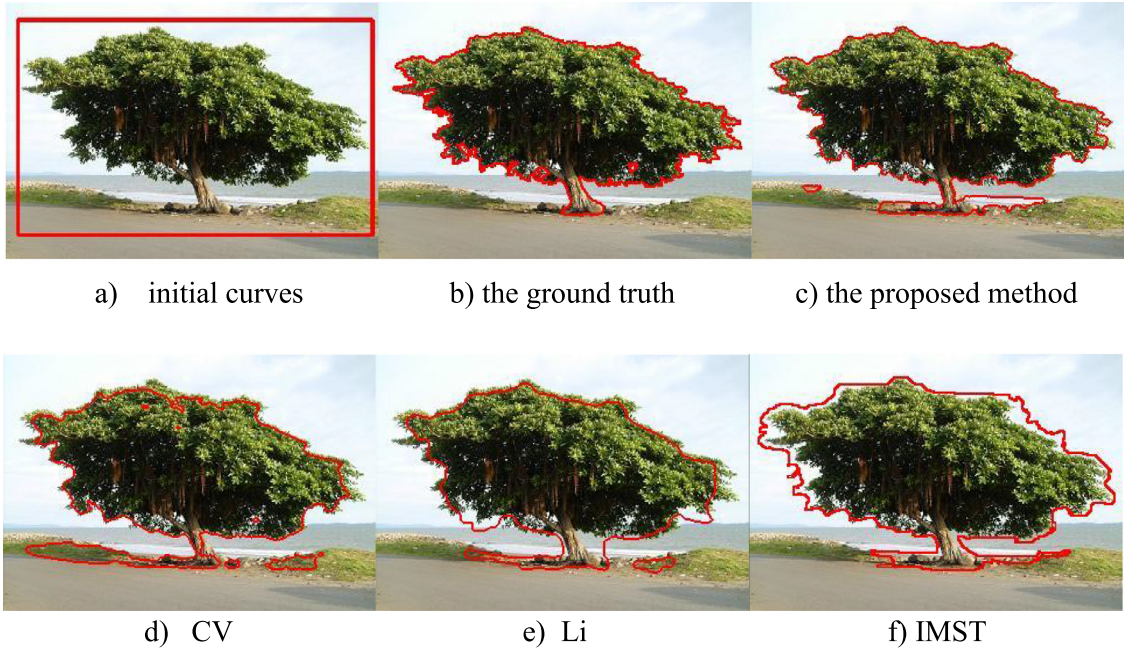

Fig. 9. Comparison of the segmentation method on the image 'the tree'.

To test segmentation performance using the proposed method on the real images, the experiments are carried on to compare with baseline model Chan and Vese (Chan and Vese, 2001b) active contour model-CV, as well as two other existing methods, Chunming Li's (Li et al., 2005) level set model-Li and Janakiraman (Janakiraman and Chandra Mouli, 2008)-IMST. The partial results are shown in Figs. 7–11. The CPU time and score of segmentation of the methods are given in Table 2. Except the IMST method, the effects of the methods on the slightly inhomogenous image are almost the same, such as Figs. 7–9. However, on images with severe inhomogeniety(as Figs. 10 and 11), the effect of the proposed method is better than the others. On Fig. 11, the locations of two persons contour using the CV model and the Li model are far away from the true boundaries, and even worse in IMST model.

Compared to the other three models, the effect of the proposed method is better. On the number of the smoothing, Li's model only needs one time Gaussian smoothing, Chan and Vese model does not smooth, but the proposed method uses iteration smoothing to achieve a better result. So the computation time is costly. On the same size images with the different inhomogeneity, the computation time mainly depends on the degree of the regional inhomogeneity. For example, the CPU time of Fig. 7 is 9.762 s, and it is 41.345 s in Fig. 11.

The noise is a major factor which leads to inhomogeneous intensity. To test if this algorithm is insensitive to noise, we segment degraded images with additive white noise, partial results are shown in Fig. 12. The initial contours are the same in Li,CV and the proposed model. The scores of segmentation on images with noise are listed in Table 3.

In Table 3, on the image without noise, the F-measure, precision and recall of image segmentation using the three methods are almost equal. However, for noisy images, the difference of segmentation score using the different methods is larger.

In order to test the ability of handling noise, we take the score of segmentation on the image without noise as a bench-

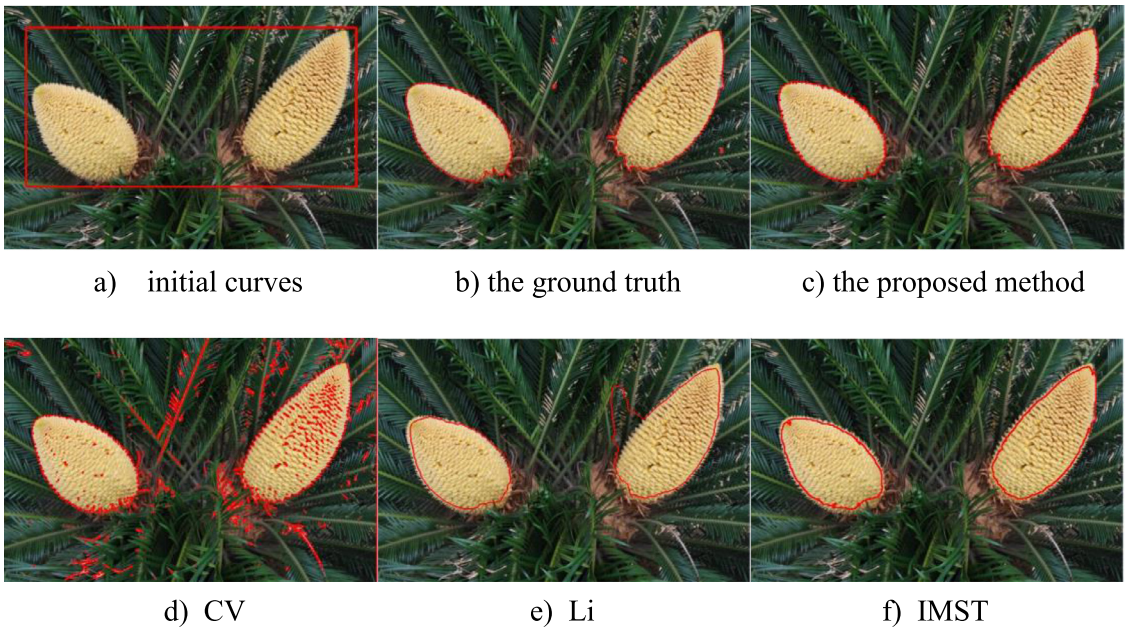

Fig. 10. Comparison of the segmentation method on the image 'the cycas'.

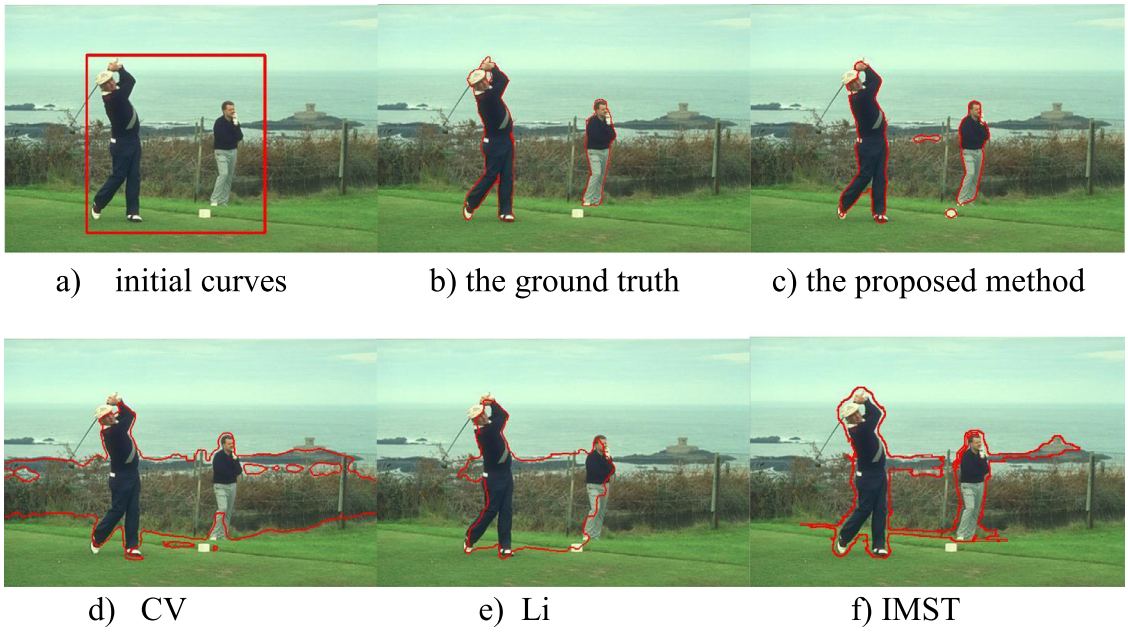

Fig. 11. Comparison of the segmentation method on the image 'two persons'.

Table 3
Score of segmentation comparison of image with noise (where *Pre, Rec, F-M* denote precision, recall and F-Measure, respectively).

PSNR(dB)	Method											
	The proposed method			The Li's model			The CV model			The IMST model		
	Pre	*Rec*	*F-M*	*Pre*	*Rec*	*F-M*	*Pre*	*Rec*	*F-M*	*Pre*	*Rec*	*F-M*
22.70	0.995	0.947	0.970	1.0	0.974	0.987	0.997	0.916	0.955	0.996	0.952	0.984
21.23	0.996	0.946	0.970	1.0	0.970	0.985	0.996	0.927	0.957	0.995	0.950	0.969
20.25	0.996	0.946	0.970	1.0	0.968	0.985	0.992	0.920	0.955	0.986	0.947	0.962
18.85	1.0	0.942	0.970	0.963	0.941	0.952	0.992	0.917	0.953	0.964	0.921	0.955
17.07	1.0	0.941	0.970	0.942	0.936	0.939	0.955	0.922	0.938	0.942	0.918	0.921
15.54	1.0	0.941	0.970	0.871	0.911	0.891	0.925	0.841	0.881	0.850	0.871	0.862
14.78	0.998	0.927	0.961	0.831	0.891	0.859	0.858	0.927	0.891	0.825	0.851	0.810
12.69	0.874	0.947	0.909	0.758	0.818	0.787	0.625	0.961	0.758	0.632	0.819	0.788
12.13	0.778	0.962	0.860	0.718	0.769	0.743	0.637	0.953	0.763	0.617	0.803	0.752
Without noise	0.995	0.948	0.971	1.0	0.983	0.992	0.985	0.953	0.968	0.995	0.952	0.985
MD	0.217	0.021	0.111	0.282	0.214	0.249	0.348	0.036	0.210	0.379	0.149	0.233
SD	0.076	0.009	0.038	0.108	0.072	0.089	0.146	0.033	0.080	0.148	0.058	0.088

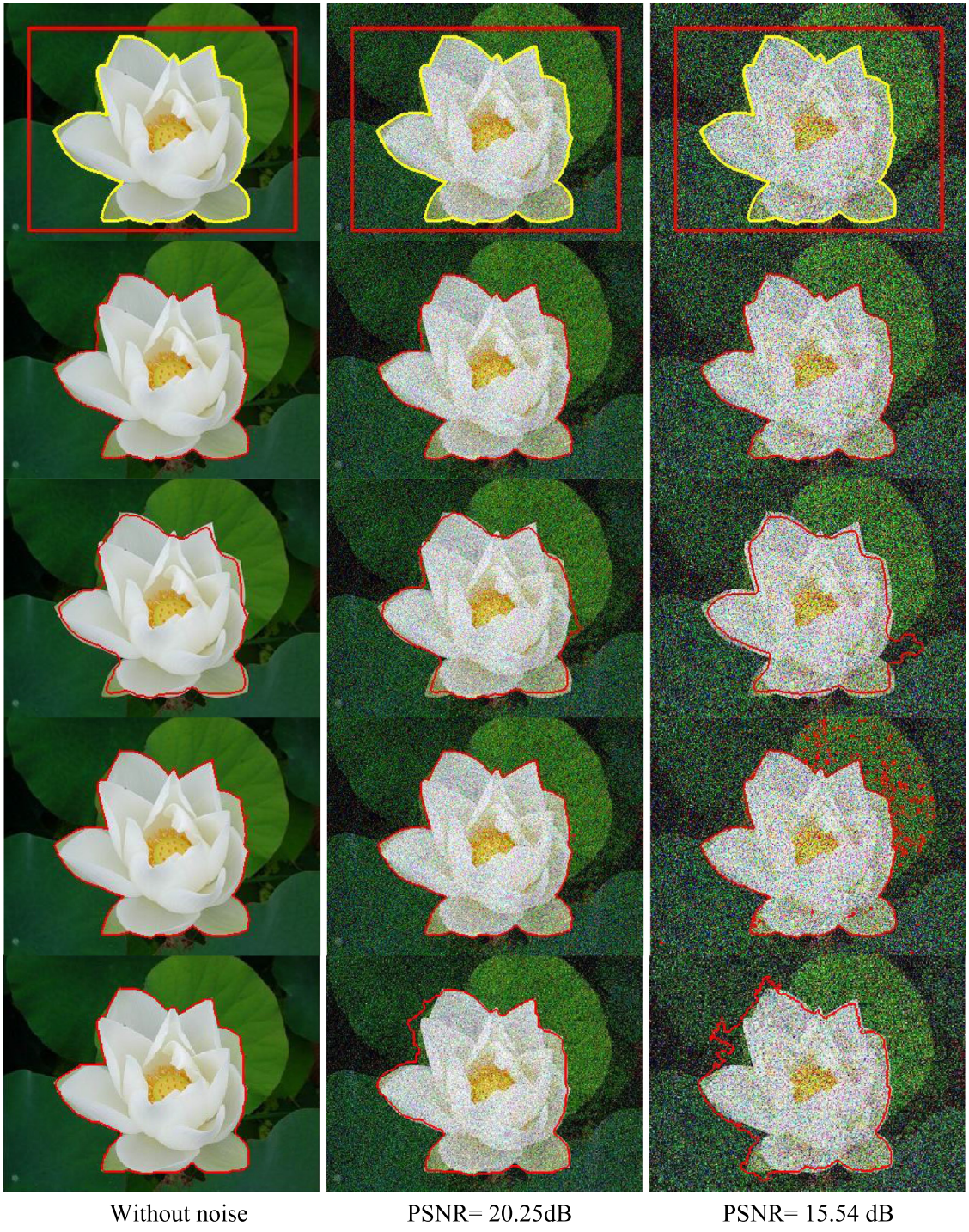

Fig. 12. Comparison of the proposed method with the Li, CV on real images with noise. *Row1* initial curves (red) and the ground truth (yellow), *Row2* segmentation results of the proposed model, *Row3* segmentation results of the Li, *Row4* segmentation results of the CV, *Row5* segmentation results of the IMST. (For interpretation of the references to color in this figure legend, the reader is referred to the web version of this article.)

mark. The maximum difference (MD) of F-measure using the proposed method is 0.111. The MD of model Li, CV and IMST are 0.249, 0.210, 0.233, respectively. The MD using the proposed method is smaller than that of the other three models, which shows that the proposed method performs well on images with noise. The standard deviation (SD) of F-measure using the proposed method is 0.038, while that of Li, CV and IMST are 0.089, 0.080, 0.088, respectively. The standard deviation using the proposed method is smaller than that of other models, this algorithm is insensitive to noise.

Although the proposed method is insensitive to noise, the computer time is longer than the other models. In the proposed method, the lower the PSNR, the longer the CPU time. The CPU time comparison of segmentation on an image with noise is shown in the Table 4.

The proposed method just uses the gradient of luminance component, but neglects the chroma variation. Some failed examples are shown in Fig. 13. Some failed segmentation was caused by the chroma gradient and strong edges within the initial contour. For example, partial boundaries of the penguin are formed by the

Table 4
CPU time (in second) comparison of segmentation on image with noise.

PSNR (dB)	22.70	21.23	20.25	18.85	17.07	15.54	14.78	12.69	12.13	Without noise
The proposed method	6.381	6.393	7.643	7.782	7.925	10.154	10.911	11.232	12.373	4.932
Li model	4.971	5.083	6.115	6.332	6.542	8.391	9.773	10.187	10.574	3.666
CVmodel	3.822	3.887	4.134	4.657	4.774	5.393	5.413	5.991	6.353	3.526
IMST	1.913	1.920	1.921	1.924	1.926	2.011	2.025	2.198	2.202	1.894

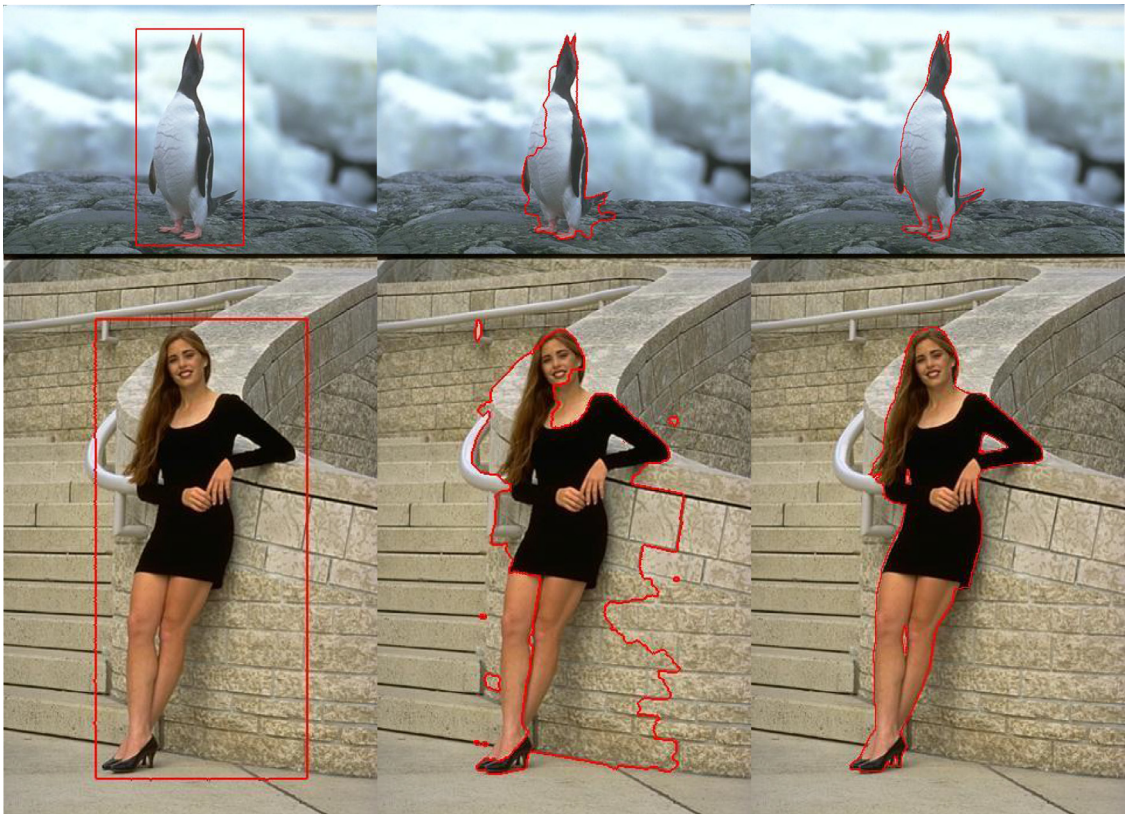

Fig. 13. Some examples of our method with weak performance.

chroma gradient, and there are strong edges in the initial contour of the girl.

6. Concluding remarks

In order to improve the traditional models performance for real images, and to combine it with the classical level set, the new image segmentation model is proposed. Compared to the comparison methods above, the proposed method is insensitive to noise and can deal with inhomogeneous sub-regions. However, the proposed method just uses the gradient of image luminance component, but neglects the chroma gradient. The computation is costly due to the gradient descent algorithm. We plan to discuss in the future how to fuse luminance and chroma gradient further, to promote the quality of image segmentation, and to solve the partial difference equation by using a conjugate gradient in order to reduce the computational time.

Acknowledgment

This work was supported by the Sichuan Province Natural Science Foundation of China (2013SZ0157).

References

Andersson, T., Läthén, G., Lenz, R., Borga, M., 2013. Modified Gradient Search for Level Set Based Image Segmentation. IEEE Trans. Image Process. 22 (2), 621–630.
Cha, K, Kim, S., 2005. MPEG-4 STUDIO: an object-based authoring system for MPEG-4 contents. Multimedia Tools Appl. 25 (January (1)), 111–131.
Chan, T.F., Osher, S., Shen, J.H., 2001. The digital TV filter and nonlinear denoising. IEEE Trans. Image Process. 10 (February (2)), 231–241.
Chan, T.F., Vese, L., 2001a. A Level set algorithm for minimizing the mumford-shah functional in image segmentation. In: Proc. of IEEE Workshop on Variational, Geometric and Level Set Methods in Computer Vision, pp. 161–168.
Chan, T.F., Vese, L., 2001b. Active contours without edges. IEEE Trans. Image Process. 10 (2), 266–277.
Evans, L., 1998. Partial Differential Equations. Providence: American Mathematical Society.
Janakiraman, T.N., Chandra Mouli, P.V.S.S.R., 2008. Image segmentation based on minimal spanning tree and cycles. In: Conference on Computational Intelligence and Multimedia Applications, 2007. International Conference on, 3, pp. 215–219.
Kass, M, Witkin, A., Terzopoulos, D., 1988. Snakes, active contour model. Int. J. Comput. Vis. 321–331.
Khan, M.W., 2014. A survey: image segmentation techniques. Int. J. Future Comput. Commun. 3 (2), 89–93.
Li, C., Kao, C., et al., 2007. Implicit active contours driven by local binary fitting energy. In: Proceedings of IEEE Conference on Computer Vision and Pattern recognition, pp. 1–7.
Li, C., Kao, C., et al., 2008. Minimization of region-scalable fitting energy for image segmentation. IEEE Trans. Image Process. 17 (10), 1940–1949.

Li, C, Xu, C., Gui, C., Fox, M.D., 2005. Level set evolution without re-initialization: a new variational formulation. In: Proceeding of the 2005 IEEE Computer Society Conference eon Computer Vision and Pattern Recognition (CVPR'05), 1, pp. 430–436.
Mumford, D, Shah, J., 1989. Optimal approximations of piecewise smooth functions and associated variational problems. Commun. Pure Appl. Math. 42, 577–685.
Peng, Y, Liu, F, et al., 2012. A normalized local binary fitting model for image segmentation. In: 4th International Conference on Intelligent Networking and Collaborative Systems, pp. 77–80.
Peng, Y, Liu, F, et al., 2014. Active contours driven by normalized local image fitting energy. J. Syst. Eng. Electron. 25 (April (2)), 307–313.
Shen, J.B., Du, Y.F., Li, X.L., 2014. Interactive segmentation using constrained laplacian optimization. IEEE Trans. Circuits Syst. Video Technol. 24 (7, July), 1086–1099.
Tsai, A, Yezzi, A, et al., 2001. Curve evolution implementation of the Mumford–Shah functional for image segmentation, denoising, interpolation, and magnification. IEEE Trans. Image Process. 10 (August (8)), 1169–1186.
Tsai, A., Yezzi, A., Willsky, A.S., 2001. Curve evolution implementation of the Mumford–Shah functional for image segmentation, denoising, interpolation, and magnification. IEEE Trans. Image Process. 10 (August (8)), 1169–1186.
Vese, L, Chan, T, 2002. A multiphase level set framework for image segmentation using the Mumford and Shah model. Int. J. Comput. Vis. 50 (3), 271–293.
Vese, L, Osher, S., 2004. Image denoising and decomposition with total variation minimization and oscillatory functions. J. Math. Image Vis. 20, 7–18.
Wang, L, Hua, G., Xue, J., Gao, Z., 2014. Joint segmentation and recognition of categorized objects from noisy web image collection. IEEE Trans. Image Process. 23 (September (9)), 4070–4086.
Xiao, Q, Jianshuai, W, Xiaoying, R, 2014. The study and application of the improved region growing algorithm for liver segmentation. Optik-Int. J. Light Electron Opt. 18 (1), 1–6.
Yang, X., Gao, X., Tao, D., Li, X., 2014. Improving level set method for fast auroral oval segmentation. IEEE Trans. Image Process. 23 (July (7)), 2854–2865.
Yeo, S.Y., Xie, X.H., Sazonov, I., Nithiarasu, P., 2013. Segmentation of biomedical images using active contour model with robust image feature and shape prior. Wiley. Int. J. Numer. Methods Biomed. Eng. 30, 232–248.
Yeo, S.Y., Xie, X.H., Sazonov, I., Nithiarasu, P., 2014. Segmentation of biomedical images using active contour model with robust image feature and shape prior. Int. J. Numer. Methods Biomed. Eng. 30, 232–248.